Dependence of the parallel mean free path of high-energy galactic cosmic rays in the heliosphere on their rigidity, and solar activity as measured by the GRAPES-3 experiment

H. Kojima, T. Koi, A. Oshima, S. Shibata, T. Tabata, H. Takamaru, and K. Yamazaki
College of Engineering, Chubu University, Kasugai, Aichi 487-8501, Japan

S. K. Gupta,* B. Hariharan, P. Jagadeesan, A. Jain, P. K. Mohanty, S. D. Morris, P. K. Nayak, K. Ramesh, M. Rameez, B. S. Rao, L. V. Reddy, and M. Zuberi
Tata Institute of Fundamental Research, Mumbai 400 005, India

Y. Hayashi and S. Kawakami
Graduate School of Science, Osaka Metropolitan University, Osaka 558-8585, Japan

T. Nakamura
Kochi University, Kochi, 780-8072, Japan

T. Nonaka and S. Ogio
Institute for Cosmic Ray Research, University of Tokyo, Kashiwa, Chiba 277-0882, Japan

K. Tanaka
Graduate School of Information Sciences, Hiroshima City University, Hiroshima 731-3194, Japan

(Received 28 August 2023; accepted 6 February 2024; published 8 March 2024)

In recent times the role of space weather on the functioning of the Earth- and space-based technological systems is attracting increasing attention due to the recognition of its potential to adversely impact those systems, especially during the extreme geomagnetic storms. On the other hand, the effects of space weather on the propagation of the galactic cosmic rays (GCRs) can be used to probe the parameters characterizing the space weather. Within the heliosphere, the embedded turbulent magnetic field in the solar wind creates a radial density gradient in an otherwise isotropic distribution of the GCRs. The diffusion-convection framework predicts that the variations in the GCR intensity, and the solar wind velocity should be anti-correlated. In the work presented here, these measurements are extended to the GRAPES-3 data collected over a long interval of 22 years from 2000 to 2021. The "HK" parameter is defined as the magnitude of ratio of the rate of change of muon intensity relative to that of the solar wind velocity. Here, the radial diffusion coefficient κ_{rr}, and the parallel mean free path $\lambda_{\|}$ have been inferred based on several simplifying assumptions, along nine independent directions each of which corresponds to a different median GCR rigidity. Each of these parameters including the HK show a strong correlation with the F10.7 Index, which is an excellent proxy for the 11 year solar activity. This possibly is the first measurement of the parameters that influence the transport of GCRs in the heliosphere, and their dependence on the solar activity at relatively high-median rigidities (64–92 GV) by a ground-based instrument. These measurements should put the link between the space weather, and the high-rigidity GCRs on a much sounder footing, and sheds some light on the complex relationship among the parameters that characterize the space weather.

DOI: 10.1103/PhysRevD.109.063011

I. INTRODUCTION

The term "solar wind" is used to describe the flow of magnetized plasma comprising primarily of protons and electrons that continually stream out from the solar corona into the heliosphere. The heliosphere spans a volume of interplanetary space where the irregularities in the outward flowing solar wind obstructs the inflow of galactic cosmic rays (GCRs). An extremely high electrical conductivity of the solar plasma results in the freezing of the interplanetary magnetic field (IMF) in the plasma. The anchoring of solar wind to the surface of the Sun combined with the solar

*gupta.crl@gmail.com

 © 2024 American Physical Society

rotation deforms the IMF into a spiral pattern. The outward convection due to the solar wind combined with the inward diffusion of the GCRs along the direction of IMF into the heliosphere disrupts their isotropy in the interstellar space. Furthermore, the motion of the GCRs is also affected by the gradients, drifts, as well as by the movement, and shape of the heliospheric neutral current sheet [1,2].

The studies of the interplanetary medium including the solar wind, and the IMF provide key information on the space weather. The importance of space weather stems from its role in triggering various physical processes in the near-Earth environment that include on rare occasions extreme geomagnetic storms that can disrupt the operation of space- and ground-based technological assets [3]. Such extreme space weather events are known to have been the root cause of disruptions of the electrical grids and communication satellites in the past. These extreme events could even endanger the lives of the astronauts in space [4]. The space weather is largely driven by the solar wind accompanied by large changes in its velocity i.e., the solar wind velocity (V_{SW}) that can be particularly devastating for modern technological systems [5].

The magnetic field and its fluctuations, frozen in the solar wind, are carried outward from the Sun with the solar wind, and that influences the diffusion of the GCRs in the heliosphere. Thus, the study of the correlation of V_{SW} with the GCR intensity offers an especially powerful probe of the space weather. Furthermore, the solar wind also affects the geomagnetic field, as well as our atmosphere through a set of complex processes. The existence of an intimate but poorly understood connection between the space weather and its influence on the Earth is the primary motivation for the launch of a large number of civilian satellites by different space agencies in the world for the monitoring of the space weather [6–8].

The plasma present in space exhibits turbulence over a large range of spatial dimensions. The GCRs propagating in turbulent magnetic fields in the plasma have an important role in providing key insights into those astrophysical environments. Some of these effects include the solar modulation of GCRs, their acceleration, and transport, as well the creation of various anisotropies. It needs to be emphasized that the process of diffusion of the GCRs in the turbulent medium of plasma is not a very well-understood phenomenon [9]. The studies of solar variability on different timescales plays an important role in determining the space weather. Such studies on timescales of centuries have relied on the records of sunspot number over several millennia, on the concentrations of the cosmogenic isotopes ^{14}C and ^{10}Be etc., in the terrestrial archives [10].

Although, in the past, the diffusion-convection framework [11–13] has been successfully employed to elucidate the propagation and modulation of the GCRs within the heliosphere. Yet, modeling the transport of GCRs in the heliosphere represents a major challenge in the field of heliospheric physics, in that such a study, if it were to be performed from first principles, requires a careful modeling of both the large-scale heliospheric plasma quantities including the heliospheric magnetic field and small-scale plasma quantities, such as various turbulence-related quantities [14].

Predictions of the diffusion-convection framework include: (i) an anticorrelated variation of the GCR intensity and the solar wind velocity (V_{SW}); (ii) the emergence of a radial density gradient in the intensity of GCRs in the presence of an IMF that leads to a GCR flow orthogonal to the plane of the ecliptic, termed "Swinson flow". By analyzing the GRAPES-3 muon data of 6 years (2000–2005), the radial diffusion coefficient κ_{rr} was derived by employing the above two predictions of the diffusion-convection framework, namely: (1) anticorrelation of the V_{SW} and the GCR intensity; (2) GCR radial density gradient from the Swinson flow. These two methods yielded nearly same values of $\kappa_{rr} = 10^{19}$ m^2 s^{-1} [15]. Hereafter, the more direct method (1) is used. In the work presented here, the older measurements based on data of 6 years have been extended to 22 years (2000–2021). Furthermore, the values of radial diffusion coefficient κ_{rr} and the parallel mean free path $\lambda_{\parallel}$ of the GCRs have been calculated for the rigidity range of 64–92 GV and as a function of the solar activity.

Despite the existence of above mentioned anticorrelation, the presence of periodic (27 day rotation, annual, 11 year activity, 22 year solar magnetic cycle), and aperiodic solar phenomena [Forbush decreases (FDs) and ground-level enhancements (GLEs)] can disrupt this delicate correlation. The influence of the periodic solar phenomena is minimized by the innovative use of indirect high-pass filters. Similarly, the contributions of the aperiodic phenomena are eliminated by selectively removing the affected data with the aid of information obtained from several neutron monitors [7,8] as described in detail in Sec. III.

The GCRs, through their interactions in the atmosphere, produce secondary particles including neutrons and muons. Neutrons by their virtue of being neutral and muons due to their ability to penetrate deep into the atmosphere, manage to reach the surface of the Earth. Therefore, these two secondary components of the GCRs can be readily studied by the ground-based instruments. Any phenomenon occurring in the interplanetary space that influences the intensity of GCRs would also be manifested through the variations in the intensity of the neutrons and/or muons at ground level. It is known that the radial density gradient of GCRs reflects the mean value of V_{SW} and κ_{rr}. The V_{SW} is also known to display rapid changes in its magnitude and consequently the measurements of the variation in the muon intensity provide an incisive probe of the space weather, wherein the muons serve as the proxy for the progenitor GCRs. Consequently, hereafter the terms "muon intensity" and "GCR intensity" are used interchangeably [7].

The correlated variations of V_{SW} and GCR intensity (with neutrons as proxy) have been extensively studied in the past, especially during the active solar phases. Some of this early work showed that the fast streams originating in the solar coronal holes were responsible for the reduction of GCR intensity [16–18]. The first use of 27 day high-pass filter to observe such an anticorrelation during a solar maximum was reported by Fujimoto *et al.* [19]. Later, similar results were reported during the coronal mass ejections (CMEs) by other groups [20]. However, the earlier correlation studies focused on the role of active regions and/or major episodic events such as the solar flares, CMEs, etc. that could have brought about such correlated variations between V_{SW} and the GCR intensity. However, such unusual circumstances are avoided in the present work (as also explained above) by studying this correlation during relatively undisturbed conditions by excluding the data influenced by FDs, GLEs, as well as by filtering the data to remove various periodic phenomena. Here, the objective is that if this correlation could be studied under relatively quiet solar conditions and the variation of the radial diffusion coefficient κ_{rr}, and parallel mean free path $\lambda_{\parallel}$ is measured as a function of the median rigidity, at different levels of solar activity, then a fundamental tenet of the space weather would have been placed on a more quantitative footing. As before, the data from the GRAPES-3 experiment with its large-area (560 m^2) muon telescope [21] that allowed tiny variations in the muon intensity to be accurately measured have been used in the present study.

In an earlier study, the GRAPES-3 muon data from the vertical direction recorded during a solar quiescent phase was used to calculate the rate of change of the GCR intensity relative to that of the solar wind velocity, after averaging over a span of 6 years (2000–2005). This analysis yielded a slope of $(-1.33 \pm 0.07) \times 10^{-5}$ km^{-1} s with a statistical significance of 19σ [7]. The magnitude of this slope is defined as the HK parameter. By using this value of the HK parameter, and a characteristic correlation length of 0.864 au obtained from the same data, the value of the radial diffusion coefficient was found to be, $\kappa_{rr} = 0.97 \times 10^{19}$ $m^2\,s^{-1}$ at 1 au [15]. Although, that analysis clearly showed the anticorrelation of the GCR intensity and the solar wind velocity V_{SW} [7], the underlying physical process(es) and/or mechanism(s) responsible for these correlations have yet to be adequately deciphered. In the present work, the scope of the analysis is expanded to include the dependence of this anticorrelation on the solar activity as well as the median GCR rigidity by analyzing the GRAPES-3 data collected over 22 years (2000–2021).

Here, it needs to emphasized that although the radial diffusion coefficient κ_{rr} of GCRs has usually been calculated from their radial density gradient [8], the GRAPES-3 measurements have shown that the value of κ_{rr} at 1 au derived from (i) the correlated variations of V_{SW}, and muon intensity (I_μ), and (ii) the radial density gradient are nearly the same, i.e., 0.97×10^{19} $m^2\,s^{-1}$ and 1.04×10^{19} $m^2\,s^{-1}$, respectively [15]. Consequently, it was decided to employ only one of these methods in the subsequent calculations of κ_{rr}. Due to a somewhat direct nature of the correlated variations of the V_{SW} and I_μ, method (i) has been preferred for further analysis.

The solar radio flux at a wavelength of 10.7 cm (2800 MHz) called the "F10.7 Index", and hereafter F10.7, is an excellent indicator of the solar activity. The F10.7 radio emission originates high in the chromosphere, and low in the corona of the solar atmosphere. The F10.7 correlates extremely well with the sunspot number (correlation coefficient > 0.99) and with a number of ultraviolet, and visible solar irradiance records. The F10.7 is one of the longest running records of solar activity, and has been measured consistently since 1947. Unlike many solar indices, the F10.7 can be easily and reliably measured on a day-to-day basis from the surface of the Earth in all types of weather conditions, and, unlike the sunspot number, the F10.7 provides an objective, and quantitative measure of the solar activity. In view of the above facts, the F10.7 is used as a reliable proxy for the solar activity [22].

II. GRAPES-3 EXPERIMENT

The GRAPES-3 experiment is being operated in Ooty, India (11.4°N latitude, 76.7°E longitude, 2200 m altitude). It comprises of two main detector systems. The first system consists of an extensive air shower (EAS) array of 400 plastic scintillator detectors with a separation of 8 m between the two adjacent detectors. Each scintillator detector has an area of 1 m^2 and is placed in a symmetric hexagonal grid [23,24]. The EAS array is designed to study the composition of GCRs in the 10 TeV–10 PeV energy range [21,25–27].

The second detector system consists of a large area (560 m^2) muon telescope comprising of 16 modules, each 35 m^2 in area. The basic detection element of the muon telescope is a proportional counter (PRC) constructed from a 600 cm long square steel tube with a wall thickness of 2.3 mm and a square cross section of 10 cm × 10 cm. Each 35 m^2 module contains 232 PRCs arranged in four layers of 58 PRCs each and the successive layers are aligned in mutually orthogonal directions as shown in Fig. 1. Each PRC layer is separated from the next by a 15 cm thick layer of concrete. Consequently, the vertical separation of the two PRC layers in the same projection plane is about 50 cm, allowing the reconstruction of the muon direction with a precision of ∼4° on an average.

The large area of the muon telescope allows the variations in the directional intensity of muons to be measured with a fairly high degree of accuracy (∼4°). A total concrete thickness of ∼550 g cm^{-2} above the Layer-0 as shown in Fig. 1 results in a threshold energy of 1 GeV for the vertical muons and the threshold varies as $\sec(\theta)$ GeV

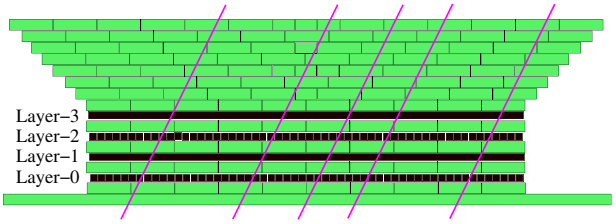

FIG. 1. A schematic view of one of the 4-layer muon telescope module with 58 PRCs in each layer, labeled Layer-0, Layer-1, … are embedded in the concrete absorber. The inclined lines represent five parallel through going muons.

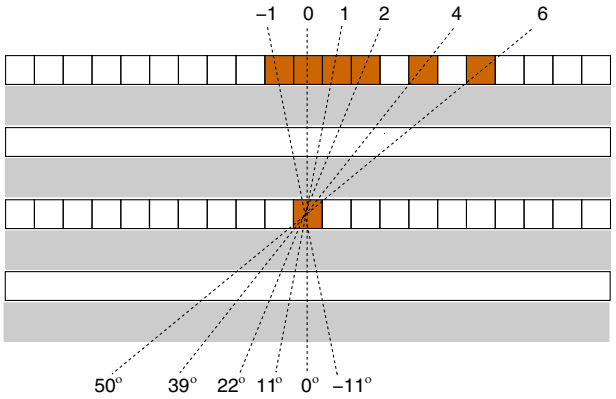

FIG. 2. A schematic view of the muon direction reconstruction based on the pair of triggered PRCs, first PRC in the lower and the second from among the 13 PRCs in the upper layer. As an example, the triggered PRCs are shown as filled squares. The dashed lines represent the reconstructed directions of six muons.

for the muons arriving at an angle θ with respect to the vertical direction. The muon direction is calculated for each triggered PRC in the lower layer and binned into 13 discrete directions based on the location of the PRC triggered in the upper layer from among 13 PRCs, one directly above (central PRC) and six PRCs on either side of the central PRC as shown in Fig. 2. This procedure is carried out for each pair of parallel projection planes that eventually leads to the creation of a sky map of muon intensity into $13 \times 13 = 169$ solid angle directions as shown in Fig. 3. The number of muons in each direction is recorded once every 10 s [28–30].

To further reduce the statistical fluctuations, the 169 directions are combined into nine "broad" directions as displayed in Fig. 3. This task is carried out by combining a group of four (E, W, N, S) 3×5 and four (NE, NW, SE, SW) 5×5 directions, with the exception of the vertical (V) direction, where the central 3×3 directions are combined. This procedure results in a relatively similar solid-angle coverage by each of the nine directions, as well as a significant reduction in the dissimilarity of the muon intensity among these directions. The geomagnetic cutoff rigidity at Ooty varies from 14 GV in the West to 23 GV in the East and is 17 GV in the vertical direction. The median rigidity of the GCRs that produced the detected muons varies in each direction, and was calculated with the aid of Monte Carlo simulations. The values of the median rigidities for the nine directions are listed in Table I in an ascending order.

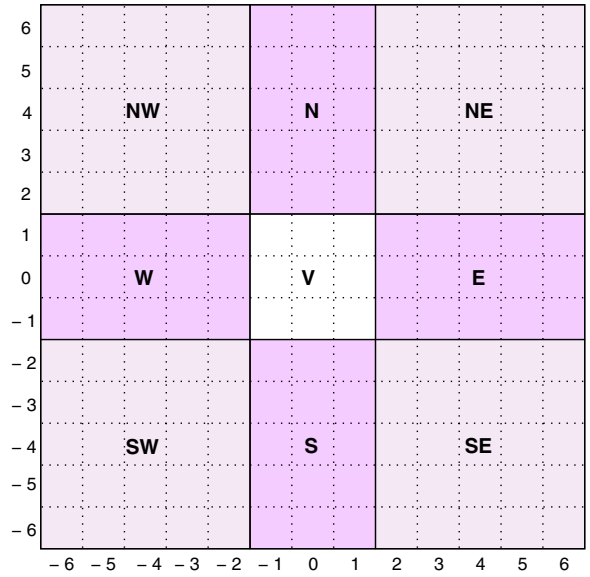

FIG. 3. A schematic of the 169 muon directions and their subsequent combinations into nine "broad" directions. These nine directions include a 3×3 vertical direction labeled V, four 3×5 central (labeled N, E, W, S), and four more 5×5 outer directions (labeled NE, SE, SW, NW). The total field of view of the muon telescope is 2.3 sr.

III. DATA ANALYSIS AND DISCUSSION

The muons of energy ≥ 1 GeV detected in the GRAPES-3 experiment correspond to a median energy of ∼77 GeV for the GCR protons within the full 2.3 sr field of view of the GRAPES-3 muon telescope. Approximately 4×10^9 muons are detected every day, permitting the generation of an intensity map of muons of exceptionally high precision. The details of the data cuts and the analysis technique used here are described in an earlier work [7].

TABLE I. Median rigidity of GCRs in the nine directions.

Serial no.	Direction	Median rigidity (GV)
1	West	64.4
2	Vertical	66.3
3	South	69.9
4	South-west	70.0
5	North-west	73.2
6	North	73.5
7	East	82.9
8	South-east	88.7
9	North-east	92.0

As mentioned in Sec. I, the interference of unrelated periodic and aperiodic phenomena due to the seasonal variations occurring on the surface of Earth and those in the interplanetary space with the intensity of muons are methodically identified, and their contributions are systematically minimized or altogether eliminated as described next. The contribution of the periodic effects including that of the 27 day solar rotation, the annual seasonal variation, the 11 year solar cycle activity, and the 22 year solar magnetic cycle are minimized with the aid of an indirect 27 day high-pass filter. The aperiodic phenomena (FDs, GLEs, etc.) that cause irregular, short-term changes in the muon intensity are characterized by a sudden drop, followed by a gradual recovery. First, the sections of data affected by these aperiodic phenomena are identified with the aid of data from neutron monitors and then their contribution is stamped out by eliminating the affected sections of the data. The details of the specific procedure(s) employed for the removal of periodic and aperiodic phenomena are described elsewhere ([7,8], and references, therein).

The cuts described above are also applied to the GRAPES-3 data of 22 year (2000–2021) to minimize the contributions of the periodic and aperiodic effects. About 90.5% of the data (7272 days out of 8036 days) survive those cuts. Next, the data from the vertical (V) direction are analyzed for calculating the daily rate of variation of the muon intensity "ΔI_μ (%)" relative to that of the solar wind velocity "$\Delta V_{\rm SW}$". This variation in the V direction ΔI_μ (%) as a function of $\Delta V_{\rm SW}$ is shown in Fig. 4. The data are binned into 40 intervals, wherein each bin contains the data from nearly equal number of days (182 days). These data are adequately fitted by a straight line as shown in Fig. 4.

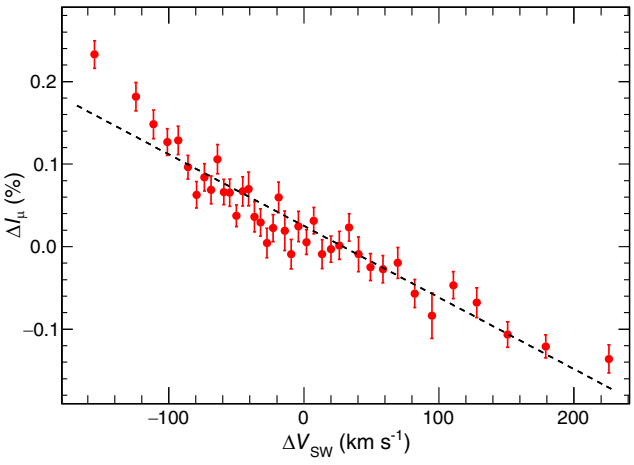

FIG. 4. Observed variation of the muon intensity "ΔI_μ (%)" in the vertical direction as a function of the variation in the solar wind velocity $\Delta V_{\rm SW}$ during the interval of 22 years. The data are binned into 40 intervals with approximately equal exposure (182 days). A linear fit to the data yield $HK = (0.867 \pm 0.031) \times 10^{-5}$ km^{-1} s.

The magnitude of slope of a linear fit to the data of 22 years defined earlier as HK turns out to be $HK = (0.867 \pm 0.031) \times 10^{-5}$ km^{-1} s. This HK value is significantly (34%) smaller than the value of $(1.33 \pm 0.07) \times 10^{-5}$ km^{-1} s reported from the previous analysis of GRAPES-3 data of 6 years (2000–2005) [7]. However, the earlier 6 year interval coincided with the peak solar activity in solar cycle 23. On the other hand, the 22 year interval (2000–2021) spans a duration equivalent to nearly two solar cycles that include most of the 23rd cycle, all of the 24th, and the start of the 25th cycle. Interestingly, the level of solar activity, when averaged over 22 year, yielded a mean F10.7 of 106 s.f.u. (solar flux unit, 1 s.f.u. $= 10^{-22}$ Wm^{-2} Hz^{-1} $= 10^4$ Jy), significantly (27%) lower than (mean F10.7 = 145 s.f.u.) during the 6 years interval used in the previous work. This observation is suggestive of a fairly strong dependence of the HK on the level of solar activity, and is in fact the primary motivation for carrying out further analysis of the GRAPES-3 data to determine the dependence of HK on the following: (i) the median rigidity of GCRs; and (ii) the level of solar activity.

Next, the dependence of HK parameter on the median rigidity R is obtained as described below. First, the HK is calculated by analyzing the dataset of 22 years separately for each of the nine directions. The median rigidity (R) in the nine directions are listed in Table I. The variation of HK as a function of the median rigidity is shown in Fig. 5. The HK displays a clear anticorrelation with the median rigidity that can be adequately described by a linear fit as shown by the dashed line in Fig. 5. This fit yields the following dependence of HK on the median rigidity R, $-\frac{\partial HK}{\partial R} = (1.2 \pm 0.1) \times 10^{-7}$ km^{-1} s GV^{-1}. It should be noted that despite an extremely small value of 1.2×10^{-7} km^{-1} s GV^{-1} $-\frac{\partial HK}{\partial R}$ could still be measured with a

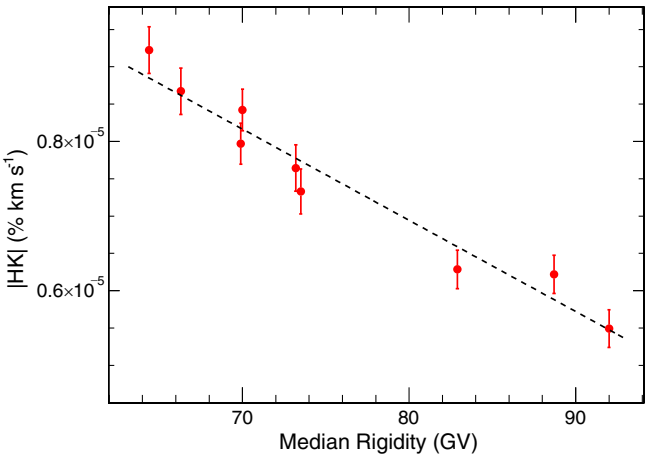

FIG. 5. The variation of HK as a function of the median rigidity R along the nine directions. The HK is anticorrelated with R, and this dependence is described by $-\frac{\partial HK}{\partial R} = (1.2 \pm 0.1) \times 10^{-7}$ km^{-1} s GV^{-1}.

TABLE II. Solar activity based grouping of the annual data.

Group no.	Year of observation	F10.7 index	Mean F10.7
1	2008	69.0	71 ± 1
	2019	69.7	
	2018	70.0	
	2009	70.5	
	2007	73.1	
	2020	73.7	
2	2017	77.3	83 ± 3
	2010	80.0	
	2006	80.0	
	2021	81.6	
	2016	88.8	
	2005	91.7	
3	2004	106.5	118 ± 4
	2011	113.3	
	2015	117.7	
	2012	120.0	
	2013	122.7	
	2003	128.4	
4	2014	145.9	172 ± 12
	2002	179.5	
	2000	180.0	
	2001	181.1	

confidence level of $\sim 12\sigma$. This measurement attests to the high sensitivity of the GRAPES-3 muon telescope in performing this delicate measurement.

Next, the simultaneous dependence of the HK parameter both on the solar activity, and the median rigidity R are computed. As described earlier, the solar activity is quantified by using the F10.7 and the data (22 years) are categorized into four groups. This classification involved sorting of the annual data according to ascending magnitude of F10.7 as summarized in Table II. This specific choice of groups is in part dictated by a hint of clustering in the magnitude of annual F10.7 during these 22 years, and partly to fulfill the requirement that approximately similar volume of data should be included in each group. The resulting classification is displayed in Fig. 6, wherein each group is circumscribed by an ellipse for easy identification. The first three groups contain the data of 6 years each, whereas the fourth group has data of only 4 years. The calculated mean F10.7 for the four groups are, (71 ± 1), (83 ± 3), (118 ± 4), and (172 ± 12) s.f.u., respectively, and these values are listed in the last column of Table II. Not surprisingly, this activity based classification results in each group containing data from nonconsecutive years, and in some cases even from different solar cycles, because the actual chronology of the data was not a criterion for this classification.

The GRAPES-3 data, after the classification into four groups as described above, are separately analyzed by first calculating the nine values of HK parameter each

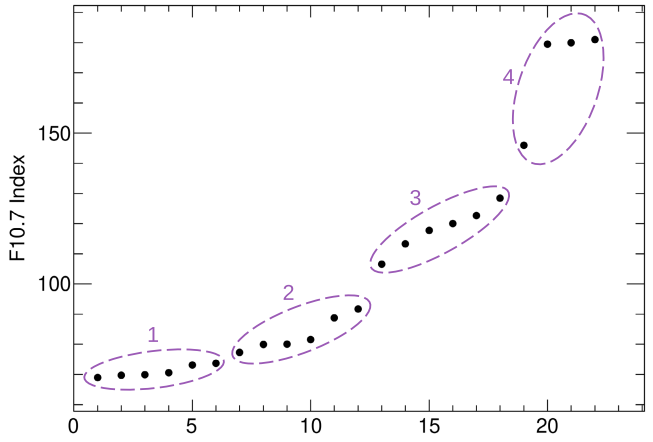

FIG. 6. Mean annual F10.7 Index plotted in ascending order, that is, each point represents the data from a single year. The data are segregated into four groups, labeled 1 through 4, and each groups is circumscribed by an ellipse for easy identification.

corresponds to a median rigidity R in that direction. For the first group this exercise yielded $-\frac{\partial HK}{\partial R} = (0.86 \pm 0.06) \times 10^{-7}$ km^{-1} s GV^{-1} as listed in Table III, which corresponds to a mean F10.7 of 71 s.f.u. Progressively, larger magnitudes of $-\frac{\partial HK}{\partial R}$ of $(1.39 \pm 0.22) \times 10^{-7}$ km^{-1} sGV^{-1}, $(1.52 \pm 0.14) \times 10^{-7}$ km^{-1} sGV^{-1}, $(1.56 \pm 0.34) \times 10^{-7}$ km^{-1} sGV^{-1} are observed for the second (83 s.f.u.), third (118 s.f.u.), and the fourth (172 s.f.u.) groups, respectively. In view of the dependence of HK both on the median rigidity R and the solar activity (F10.7), it became necessary to simultaneously display this relationship through a 3D plot as shown in Fig. 7. Here, the two independent variables, namely, R the median rigidity and F10.7 are shown along the x-, and the y-axes, respectively. The value of HK parameter which is the dependent variable is shown along the z-axis. The color-coded surface shown in Fig. 7 represents the dependence of HK on R and F10.7, respectively. The nonplanarity of this surface implies that the combined dependence of HK on these two variables is far more complex than a simple linear one. The anticorrelation between HK and R is expected, because at higher rigidities the GCRs are less influenced by the changes in the solar wind velocity. Similarly, a higher solar activity implies the presence of a stronger IMF, and that in turn is expected to produce a larger value of HK as seen from Fig. 7. This complex relationship of HK with R and F10.7 is

TABLE III. Rigidity dependence of $\frac{\partial HK}{\partial R}$.

Group no.	$-\frac{\partial HK}{\partial R}$	Significance
1	$(0.86 \pm 0.06) \times 10^{-7}$	14σ
2	$(1.39 \pm 0.22) \times 10^{-7}$	6σ
3	$(1.52 \pm 0.14) \times 10^{-7}$	11σ
4	$(1.56 \pm 0.34) \times 10^{-7}$	5σ

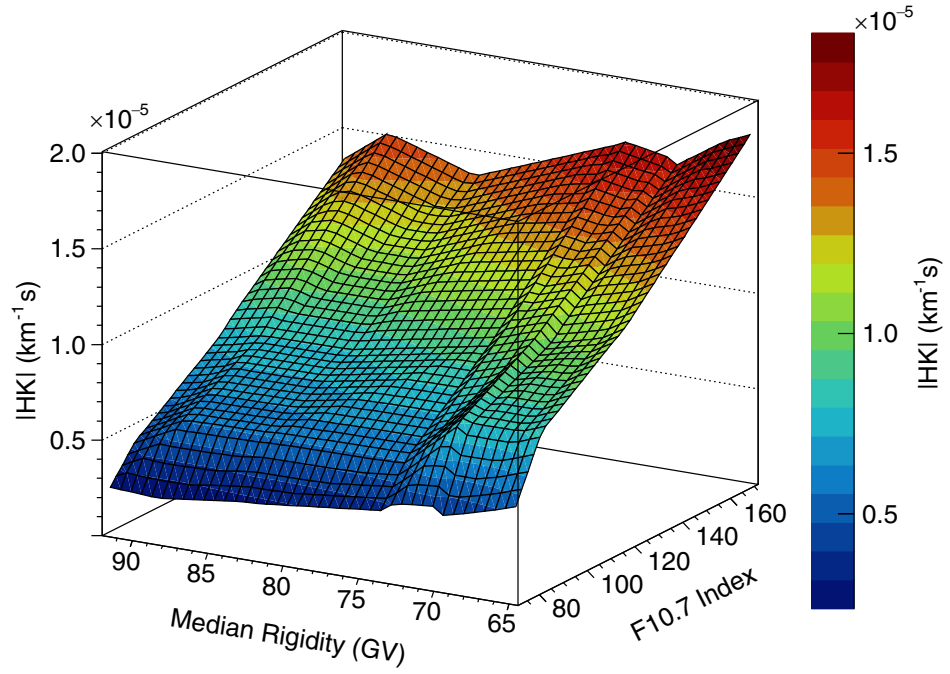

FIG. 7. HK parameter is plotted along the z-axis as a function of the median rigidity R along the x-axis and the solar activity index "F10.7" along the y-axis. HK systematically increases with, (a) decreasing R, (b) increasing F10.7. The nonplanar nature of the HK surface indicates the presence of significant nonlinearity in this relationship.

well-captured by the surface plot shown in Fig. 7. The first column in Table IV lists the solar activity based group number (1 through 4) and the second column corresponds to the mean value of F10.7. The third column contains the value of mean solar wind velocity $V_{\rm SW}$ and the fourth column the median rigidity R for the nine directions in that group.

The subsequent analysis is identical to the one used in a previous work [15]. The integral form of the diffusion-convection equation,

$$n(r) = n(r_0)\exp\left\{-\frac{v_0(r_0-r)}{\kappa_{rr}}\right\} \qquad (0 \le r \le r_0),$$

allows the variations in $V_{\rm SW}$ to be linked to those in GCR intensity, when expressed in differential form relative to the velocity "v_0" yields the HK parameter,

$$\frac{1}{n}\frac{\partial n}{\partial v_0} = -\frac{(r_0-r)}{\kappa_{rr}}$$

or

$$\kappa_{rr} = -(r_0-r)\left(\frac{\Delta n}{n\Delta v}\right)^{-1},$$

where $-\frac{\Delta n}{n\Delta v}$ is the HK parameter. The value of HK parameter varies by a factor of 8 from a low 0.216×10^{-5} km^{-1} s to 1.796×10^{-5} km^{-1} s as displayed in the sixth column of Table IV.

While the anticorrelation between the concurrent GCR intensity and solar wind velocity is used to calculate the HK parameter; however, this correlation is expected to gradually weaken with the increasing time offset between the measurements of these two parameters. By utilizing the hourly GCR data from each solar activity group, the correlation coefficient between these two parameters is calculated as a function of the time offset. By following the procedure cited in [15], the full width at half maximum of correlation coefficient termed the "correlation length" is separately calculated for each of the nine directions. The correlation length provides a fairly good measure of the size of the region "$(r_0 - r)$", where the solar wind velocity and GCRs remain correlated. The correlation length varies from a low value of 63 hours to a high of 88 hours as shown in the fifth column of Table IV. The mean solar wind velocity, shown in the third column of Table IV, is used to calculate the correlation length for that group. Similarly, the size $(r_0 - r)$ listed in each row in Table IV is used to compute the radial diffusion coefficient κ_{rr},

$$\kappa_{rr} = \frac{(r_0-r)}{HK}.$$

The computed values of κ_{rr} are shown in the eighth column of Table IV. As expected, the maximum value of the radial diffusion coefficient $\kappa_{rr} = 5.63\times 10^{19}$ m^2 s^{-1} occurs during the lowest solar activity (F10.7 = 71 s.f.u.) in the direction of the highest median rigidity (92 GV). Similarly, its minimum value of $\kappa_{rr} = 0.56\times 10^{19}$m^2 s^{-1} is observed

TABLE IV. The measurements of the HK parameter, the radial diffusion coefficient (κ_{rr}) and the parallel mean free path ($\lambda_{\parallel}$) on the median rigidity R, and on the level of solar activity as characterized by the F10.7 Index.

Group no.	F10.7 index	V_{SW} km s^{-1}	Rigidity (GV)	Correlation length (hours)	HK $\times 10^{-5}$ km^{-1} s	$(r_0 - r)$ $\times 10^{11}$ m	Diffusion coefficient κ_{rr} ($\times 10^{19}$ m^2 s^{-1})	tan(χ)	Mean free path $\lambda_{\parallel}$ (au)
1	71 ± 1	407	73.2	85	0.367	1.24	3.38	0.979	4.43
			73.5	87	0.345	1.27	3.68		4.82
			92.0	83	0.216	1.21	5.63		7.37
			64.4	80	0.477	1.18	2.47		3.23
			66.3	80	0.427	1.17	2.75		3.60
			82.9	79	0.261	1.15	4.41		5.77
			70.0	72	0.392	1.05	2.67		3.50
			69.9	72	0.350	1.06	3.03		3.96
			88.7	68	0.200	1.00	4.98		6.53
2	83 ± 3	430	73.2	72	0.601	1.12	1.87	0.927	2.32
			73.5	73	0.570	1.14	1.99		2.48
			92.0	72	0.419	1.11	2.65		3.30
			64.4	77	0.842	1.19	1.41		1.76
			66.3	78	0.784	1.21	1.55		1.92
			82.9	78	0.560	1.20	2.16		2.68
			70.0	80	0.820	1.24	1.51		1.88
			69.9	82	0.783	1.26	1.61		2.01
			88.7	81	0.550	1.26	2.29		2.85
3	118 ± 4	439	73.2	88	0.997	1.39	1.39	0.908	1.70
			73.5	86	0.947	1.37	1.44		1.76
			92.0	86	0.744	1.36	1.83		2.23
			64.4	83	1.169	1.31	1.12		1.37
			66.3	83	1.083	1.31	1.21		1.48
			82.9	83	0.804	1.31	1.63		1.98
			70.0	82	1.080	1.30	1.20		1.47
			69.9	82	1.008	1.29	1.28		1.56
			88.7	82	0.802	1.30	1.62		1.97
4	172 ± 12	418	73.2	80	1.704	1.30	0.706	0.954	0.90
			73.5	78	1.678	1.30	0.700		0.80
			92.0	73	1.344	1.09	0.812		1.04
			64.4	69	1.862	1.04	0.559		0.71
			66.3	68	1.796	1.02	0.569		0.73
			82.9	71	1.391	1.06	0.763		0.97
			70.0	63	1.658	0.95	0.570		0.73
			69.9	65	1.608	0.97	0.605		0.77
			88.7	65	1.540	0.98	0.634		0.81

during the highest solar activity (F10.7 = 172 s.f.u.) in the direction of lowest median rigidity (64 GV). The magnitude of κ_{rr} had varied by a factor of ten owing to the changes in the median rigidity and the solar activity during the 22 year interval.

Following the procedure described in [11], the angle χ between the IMF and the radial direction joining the Sun to the Earth is calculated as follows:

$$\tan\chi = \frac{2\pi r_E}{V_{SW} T},$$

where $r_E (0 < r_E < r_0)$ is the radius of the orbit of Earth (1 au) and T is the rotation period of the Sun which is taken to be 27.3 days,

$$\tan\chi = \frac{2\pi \times r_E}{V_{SW} \times 27.3 \times 86400}.$$

The computed values of $\tan\chi$ for the four solar activity groups are displayed in the ninth column of Table IV. It is to be noted that the calculated value of χ varies between 42° and 44°.

The parallel diffusion coefficient $\kappa_{\parallel}$ may be estimated from κ_{rr} as follows [31]:

$$\kappa_{\parallel} = \frac{\kappa_{rr}}{\cos^2\chi}.$$

Subsequently, by utilizing the relation between the parallel diffusion coefficient $\kappa_{\parallel}$ and the parallel mean free path $\lambda_{\parallel}$ [31],

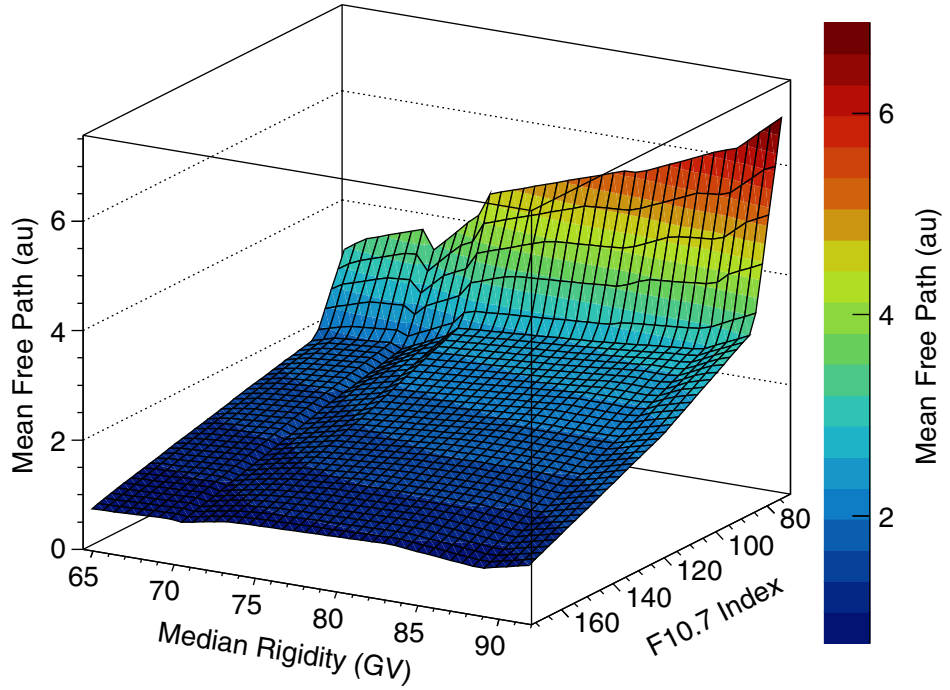

FIG. 8. The parallel mean free path $\lambda_{\parallel}$ plotted along the z-axis as a function of the median rigidity R along the x-axis, and the solar activity index F10.7 along the y-axis. First, $\lambda_{\parallel}$ gradually increases with, (a) increasing R, and (b) decreasing F10.7. However, below about F10.7 = 100 s.f.u., the rate of change of $\lambda_{\parallel}$ increases rapidly. The nonplanar nature of the $\lambda_{\parallel}$ surface indicates a nonlinear dependence on R, and F10.7 that is far more striking than in the case of HK shown in Fig. 7.

$$\lambda_{\parallel} = \frac{3\kappa_{\parallel}}{c},$$

where "c" is the velocity of light as well as that of the GCRs in the present case. The computed values of $\lambda_{\parallel}$ are shown in the last column of Table IV. Since the parallel mean free path $\lambda_{\parallel}$ scales with κ_{rr} thus, $\lambda_{\parallel}$ too varies by about a factor of 10 from a maximum of 7.4 au at the highest median rigidity (92 GV) and lowest solar activity (71 s.f.u.) to a minimum of 0.7 au at the lowest median rigidity (64 GV), and maximum solar activity (172 s.f.u.) during this span of 22 years. As discussed earlier that modeling the transport of GCRs in the heliosphere requires a knowledge of its global structure including that of the magnetic field both on the large and small scales [14]. In that context, the GRAPES-3 measurements of parallel mean free path $\lambda_{\parallel} = (0.7\text{–}7.4)$ au obtained for the median rigidity range of 64–92 GV might turn out to be fairly useful.

The variations of parallel mean free path $\lambda_{\parallel}$ as a function of the median rigidity of GCRs and the solar activity are shown in Fig. 8. As in the case of HK parameter shown in Fig. 7, the two independent variables, namely, the median rigidity R, and the solar activity (F10.7) are shown along the x- and y-axes, respectively whereas $\lambda_{\parallel}$ is shown along the z-axis. $\lambda_{\parallel}$ also displays a complex dependence on the median rigidity and solar activity. However, unlike in the case of HK where the variation occurs fairly uniformly, the bulk of variation in $\lambda_{\parallel}$ occurs at lower levels of solar activity below F10.7 = 100 s.f.u. as seen from Fig. 8.

The pioneering work of Palmer [31] was focused on a discussion of the transport of low-energy GCRs in the heliosphere, and they had also compiled the measurements of parallel mean free path $\lambda_{\parallel}$ up to a GCR rigidity of 3 GV. Subsequently, this work came to be recognized as the "Palmer consensus". However, with the advent of newer measurements at higher rigidities, and through a continually improving understanding of the GCR transport in the heliosphere the Palmer consensus has been periodically revisited and updated [14,32–34].

In a recent work, a data-driven analysis of the temporal dependence of data on monthly GCR intensity gathered over equivalent of a solar cycle by the AMS-02 and PAMELA experiments in space was performed to determine the rigidity and time dependence of the GCR parallel mean free path in the heliosphere. A global statistical inference of these data permitted the authors to interpret the GCR intensity in terms of basic processes of particle transport and their relations with the dynamics of the heliospheric plasma [35]. This approach was used to calculate the time, and rigidity dependence of parallel mean free path $\lambda_{\parallel}$. It is to be noted that the PAMELA data were recorded during relatively lower solar activity than the AMS-02 data. These two sets had a sizable overlap in time which resulted in significant overlap in the values of

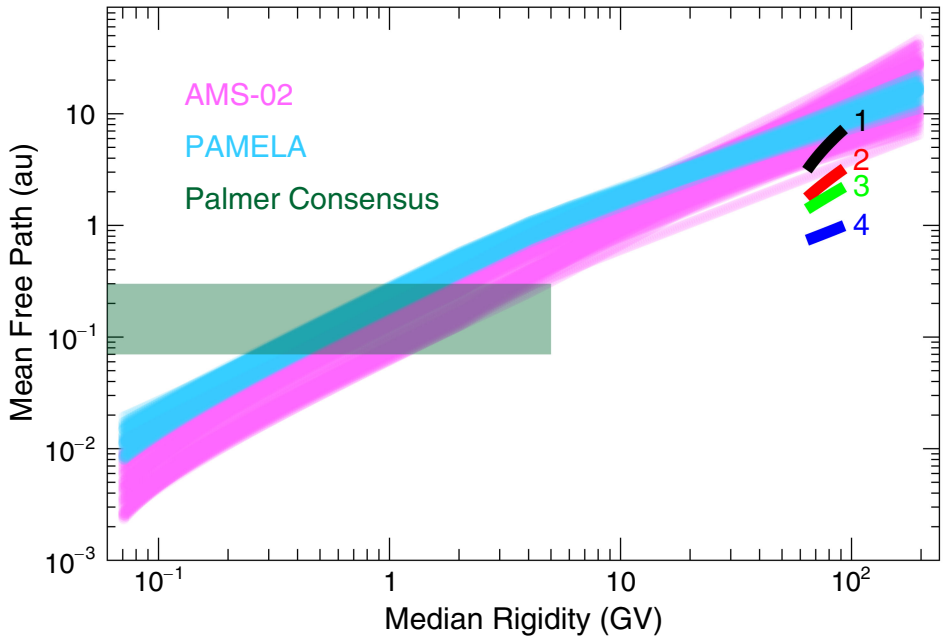

FIG. 9. The parallel mean free path $\lambda_{\parallel}$ is shown as a function of rigidity. This plot is basically a reproduction of the Fig. 4 in [36] wherein the shaded area shown in cyan, and magenta colors are based on the PAMELA, and AMS-02 data, respectively. The PAMELA data are for the interval June 2006 to March 2010, and AMS-02 data are for May 2011 to May 2017. Four short straight lines labeled 1 through 4, represent the variation of $\lambda_{\parallel}$ in the rigidity range 64–92 GV obtained from the GRAPES-3 muon data of 22 years and corresponding to progressively increasing levels of solar activity with F10.7 at 71 s.f.u., 83 s.f.u., 118 s.f.u., and 172 s.f.u., respectively, as summarized in Table II.

$\lambda_{\parallel}$ as seen from Fig. 4 in [36]. At our request, the authors generously [37] made the diffusion parameters used in the generation of fits shown in Fig. 4 [36] available. Subsequently, these parameters were reanalyzed after excluding the PAMELA data that had overlapped with the AMS-02 data. As a consequence, the selected PAMELA diffusion parameters are for the interval from June 2006 to March 2010, whereas those for the AMS-02 are from May 2011 to May 2017. The results of this reanalysis are displayed in Fig. 9. But now, the envelope of $\lambda_{\parallel}$ values as a function of the GCR rigidity inferred for the AMS-02 (magenta), and PAMELA (cyan) form two distinct bands with little overlap as seen from Fig. 9. These two bands of parallel mean free paths do not seem to be inconsistent with the Palmer consensus at low rigidities, which is shown by the shaded green box in Fig. 9 [31].

As discussed before, the median GCR rigidity for each of the nine directions, and the corresponding parallel mean free paths $\lambda_{\parallel}$ derived from the GRAPES-3 data are listed in columns four and nine, respectively, in Table IV, and they are segregated into four groups of increasing solar activity. For each group, the dependence of $\lambda_{\parallel}$ on median rigidity in the range of 64–92 GV can be adequately described by a linear fit. These linear fits corresponding to the groups labeled "1" through "4" are also shown in Fig. 9. The bottom fit for group "4" corresponds to the highest level of solar activity during four out of 22 years, displays the weakest dependence on median rigidity with a slope of (0.0090 ± 0.0029) au GV^{-1}. The fit for group "3" displays a 3× larger slope of (0.0284 ± 0.0029) au GV^{-1}. This trend continues for fit for group "2" has a 1.8 times larger slope of (0.0507 ± 0.0052) au GV^{-1}, and finally fit for group "1" has the steepest slope of (0.145 ± 0.009) au GV^{-1}. Of course, the same behavior is also reflected in Fig. 8.

The GRAPES-3 results discussed above demonstrate that the parallel mean free path $\lambda_{\parallel}$ increases with decreasing solar activity, and its dependence on the median rigidity also becomes steeper with decreasing solar activity. It may be noted that the band of $\lambda_{\parallel}$ values shown in Fig. 9 for the PAMELA experiment recorded during relatively lower solar activity are systematically larger than those for the AMS-02 experiment that were recorded during comparatively higher levels of solar activity. This behavior is entirely consistent with the quantitative variation of $\lambda_{\parallel}$ measured by the GRAPES-3 experiment. In fact, a more comprehensive analysis of the AMS-02 and PAMELA data could measure this variation of over a larger range of rigidities, and provide evidence for an unambiguous dependence of $\lambda_{\parallel}$ on the solar activity. The Palmer consensus has been a very useful tool while compiling and discussing the measurements of $\lambda_{\parallel}$ from different experiments. However, the present work goes beyond the Palmer consensus, and quantitatively

demonstrates the explicit role of solar activity in influencing the parallel mean free path $\lambda_{\parallel}$ that could serve as the next logical step in advancing our understanding of the solar modulation of GCRs and the space weather.

IV. SUMMARY

In the heliosphere the GCR intensity and the solar wind velocity are anticorrelated. The ratio of these changes termed the HK parameter has been measured by analyzing the GRAPES-3 muon data spanning 22 years (2000–2021). By exploiting the multirigidity capability of the GRAPES-3 muon telescope, the dependence of the HK on both the median rigidity (64–92 GV) and the solar activity (F10.7 71–172 s.f.u.) have been quantitatively estimated. The HK, in turn is used to derive the parameters characterizing the diffusion, and propagation of the GCRs in the heliosphere as a function of the median rigidity and solar activity. This analysis has shown that the parallel mean free path $\lambda_{\parallel}$ had varied by a factor of 10 from a maximum of 7.4 au at the highest median rigidity (92 GV) and at the lowest level of solar activity (F10.7 = 71 s.f.u.) to a minimum of 0.7 au at the lowest rigidity (64 GV) and the highest level of solar activity (F10.7 = 172 s.f.u.) during the 22 year interval of 2000–2021 studied here. The GRAPES-3 data display a linear dependence of $\lambda_{\parallel}$ on the median rigidity with a positive slope. However, starting from the lowest solar activity, the value of this slope rapidly decreases with increasing levels of solar activity, but thereafter this rate of decrease becomes more modest.

The study of the space weather through the process of diffusive propagation of high-energy GCRs is an important area of research, because it provides a probe of relatively large-scale structures in the interplanetary space ranging in sizes from 1 au to several au, that are complementary to the information obtained through lower-energy measurements by the space-borne probes. The study of space weather through the process of diffusive propagation of high-energy GCRs is an important area of research. Since the magnitude of mean free path $\lambda_{\parallel}$ of the GCRs essentially reflects the spatial dimension of space being probed, these measurements provide an indirect probe over relatively large distances of the interplanetary space ranging in sizes from 1 au to several au, that are complementary to the information obtained through lower-energy measurements by the space-borne probes with the possible exception of larger instruments such as the AMS-02 [38]. To the best of our knowledge this is the first quantitative report of the dependence of $\lambda_{\parallel}$ as a function of the median rigidity near 100 GV, as well as of its dependence on the solar activity by a ground-based instrument from the data gathered over three solar cycles. It is hoped that this information should help in a more comprehensive understanding of the space weather phenomenon over larger distances (0.7–7.4 au) over multiple solar cycles.

ACKNOWLEDGMENTS

S. K. Gupta gratefully acknowledges the award of a Department of Atomic Energy Raja Ramanna Fellowship that greatly facilitated his research. D. B. Arjunan, G. P. Francis, I. M. Haroon, V. Jeyakumar, late S. Karthikeyan, S. Kingston, N. K. Lokre, K. Manjunath, S. Murugapandian, S. Pandurangan, B. Rajesh, P. S. Rakshe, K. Ramadass, C. Ravindran, V. Santhosh Kumar, S. Sathyaraj, C. Shobana, M. S. Shareef, R. Suresh Kumar are thanked for their assistance in running the GRAPES-3 experiment. We thank Nicola Tomassetti for making the data used in generating one of his plots shown as Fig. 4 in [36] available to us, and for answering our queries. The availability of the OMNI data, as well as the Kiel, and Moscow neutron monitor data were essential for the analysis presented in this work that we gratefully acknowledge. This work was generously supported by the grants from the Department of Atomic Energy of the Government of India, and the Japanese funding agencies including the MEXT KAKENHI, the Institute for Space-Earth Environmental Research of Nagoya University, the Institute for Cosmic Ray Research, of the University of Tokyo, and the Chubu University, Kasugai.

[1] F. F. Chen, *Introduction to Plasma Physics and Controlled Fusion*, 3rd ed. (Springer, New York, 2016), https://link.springer.com/book/10.1007/978-3-319-22309-4.
[2] J. R. Jokipii, Rev. Geophys. Space Phys. **9**, 27 (1971).
[3] K. Kudela, M. Storini, M. Y. Hofer, and A. Belov, Space Sci. Rev. **93**, 153 (2000).
[4] D. N. Baker, Adv. Space Res. **22**, 7 (1998).
[5] M. L. Goldstein, D. A. Roberts, and W. H. Matthaeus, Annu. Rev. Astron. Astrophys. **33**, 283 (1995).
[6] The OMNI data obtained from the GSFC/SPDF OMNIWeb interface at https://omniweb.gsf.nasa.gov.
[7] H. Kojima, H. M. Antia, S. R. Dugad, S. K. Gupta, P. Jagadeesan, A. Jain *et al.*, Phys. Rev. D **91**, 121303(R) (2015).
[8] H. Kojima H. M. Antia, S. R. Dugad, S. K. Gupta, Y. Hayashi, P. Jagadeesan *et al.*, Astropart. Phys. **62**, 21 (2015).
[9] S. Xu and H. Yan, Astrophys. J. **779**, 140 (2013).
[10] I. G. Usoskin, Living Rev. Solar Phys. **14**, 3 (2017).

[11] E. N. Parker, Astrophys. J. **128**, 664 (1958).
[12] E. N. Parker, Planet. Space Sci. **13**, 9 (1965).
[13] E. N. Parker, Planet. Space Sci. **15**, 1723 (1967).
[14] N. E. Engelbrecht, F. Effenberger, V. Florinski, M. S. Potgieter, D. Ruffolo, R. Chhiber, A. V. Usmanov, J. S. Rankin, and P. L. Els, Space Sci. Rev. **218**, 33 (2022).
[15] H. Kojima, K. P. Arunbabu, S. R. Dugad, S. K. Gupta, B. Hariharan, P. Jagadeesan *et al.*, Phys. Rev. D **98**, 022004 (2018).
[16] N. Iucci, M. Parisi, M. Storini, and G. Villoresi, Nuovo Cimento **2**, 421 (1979).
[17] Y. Munakata and K. Nagashima, in *Proceedings of the 16th ICRC, Kyoto* (1979), Vol. 4, pp. 530–534, https://ui.adsabs.harvard.edu/abs/1979ICRC....3..530M/abstract.
[18] D. Venkatesan, A. K. Shukla, and S. P. Agrawal, Sol. Phys. **81**, 375 (1982).
[19] K. Fujimoto *et al.*, in *Proceedings of the 18th ICRC, Bangalore* (1983), Vol. 3, p. 267;, https://ui.adsabs.harvard.edu/abs/1983ICRC....3..267F/abstract; K. Fujimoto *et al.*, *Proceedings of the 19th ICRC, San Diego* (1985), Vol. 5, p. 262, https://ui.adsabs.harvard.edu/abs/1985ICRC....5..262F/abstract.
[20] E. W. Cliver, A. G. Ling, and I. G. Richardson, Astrophys. J. **592**, 574 (2003); S. Yashiro, H. Xie, and J. F. Valdés-Galicia, Astrophys. J. **625**, 441 (2005).
[21] S. K. Gupta, Y. Aikawa, N. V. Gopalakrishnan, Y. Hayashi, N. Ikeda, N. Ito, A. Jain *et al.*, Nucl. Instrum. Methods **540A**, 311 (2005); Y. Hayashi, Y. Aikawa, N. V. Gopalakrishnan, S. K. Gupta, N. Ikeda, N. Ito *et al.*, Nucl. Instrum. Methods **545A**, 643 (2005).
[22] https://www.swpc.noaa.gov/phenomena/f107-cm-radio-emissions.
[23] P. K. Mohanty S. R. Dugad, U. D. Goswami, S. K. Gupta, Y. Hayashi, A. Iyer *et al.*, Astropart. Phys. **31**, 24 (2009).
[24] P. K. Mohanty, S. R. Dugad, and S. K. Gupta, Rev. Sci. Instrum. **83**, 043301 (2012).
[25] S. K. Gupta, H. M. Antia, S. R. Dugad, U. D. Goswami, Y. Hayashi, A. Iyer *et al.*, Nucl. Phys. B, Proc. Suppl. **196**, 153 (2009).
[26] H. Tanaka, S. R. Dugad, S. K. Gupta, A. Jain, P. K. Mohanty, B. S. Rao *et al.*, J. Phys. G **39**, 025201 (2012).
[27] S. K. Gupta, Proc. Indian Natn. Sci. Acad. **80**, 827 (2014), Special Issue 4.
[28] T. Nonaka, Y. Hayashi, N. Ito, S. Kawakami, T. Matsuyama, A. Oshima *et al.*, Phys. Rev. D **74**, 052003 (2006).
[29] P. Subramanian, H. M. Antia, S. R. Dugad, U. D. Goswami, S. K. Gupta, Y. Hayashi *et al.*, Astron. Astrophys. **494**, 1107 (2009).
[30] K. P. Arunbabu, H. M. Antia, S. R. Dugad, S. K. Gupta, Y. Hayashi, S. Kawakami, P. K. Mohanty, T. Nonaka, A. Oshima, and P. Subramanian, Astron. Astrophys. **555**, A139 (2013); **580**, A41 (2015).
[31] I. D. Palmer, Rev. Geophys. Space Phys. **20**, 335 (1982).
[32] J. W. Bieber, W. H. Matthaeus, C. W. Smith, W. Wanner, M.-B. Kallenrode, and G. Wibberenz, Astrophys. J. **420**, 294 (1994).
[33] R. C. Tautz and A. Shalchi, J. Geophys. Res. **118**, 642 (2013).
[34] R. Chhiber, P. Subedi, A. V. Usmanov, W. H. Matthaeus, D. Ruffolo, M. L. Goldstein, and T. N. Parashar, Astrophys. J. Suppl. Ser. **230**, 21 (2017).
[35] E. Fiandrini, N. Tomassetti, B. Bertucci, F. Donnini, M. Graziani, B. Khiali, and A. Reina Conde, Phys. Rev. D **104**, 023012 (2021).
[36] N. Tomassetti, B. Bertucci, F. Donnini, M. Graziani, E. Fiandrini, B. Khiali, and A. R. Conde, Rend. Fis. Acc. Lincei, 10.1007/s12210-023-01149-1 (2023).
[37] Nicola Tomassetti (private Communication).
[38] https://ams02.space/.